Chemical Geology 718 (2026) 123499

Contents lists available at ScienceDirect

Chemical Geology

journal homepage: www.elsevier.com/locate/chemgeo

Research Paper

Nickel toxicity inhibits abundance and activity of cyanobacteria and Fe(III)-reducers in low-phosphate Archean oceans

Carolin L. Dreher [a], Manuel Schad [b,c], Kurt O. Konhauser [b], Andreas Kappler [a,*]

[a] Geomicrobiology, Department of Geosciences, University of Tuebingen, Tuebingen, Germany
[b] Department of Earth and Atmospheric Sciences, University of Alberta, Edmonton, Alberta, Canada
[c] GFZ Helmholtz Centre for Geosciences, Section Geomicrobiology, Potsdam, Germany

ARTICLE INFO

Editor: Yuanzhi Tang

Keywords:
Nickel
Phosphate
Cyanobacteria
Microbial Fe(II) oxidation
Great oxidation event

ABSTRACT

Banded iron formations (BIFs) are iron (Fe)- and silica (SiO_2)-rich marine chemical sediments that formed between 3.8 and 1.85 Ga, recording early ocean geochemistry and the rise of oxygen during the Great Oxidation Event (GOE, ~2.45 Ga). Cyanobacterial oxygen (O_2) production led to iron mineral precipitation, with subsequent Fe(III) reduction by dissimilatory Fe(III)-reducing bacteria (DIRB). However, the remobilization and roles of essential dissolved nutrients (phosphate, PO_4^{3-}) and micronutrients that also function as potential toxins (nickel, Ni), remain unclear. We conducted batch experiments with two consecutive Fe(II) oxidation and Fe(III) reduction cycles with the marine cyanobacterium *Synechococcus* sp. PCC7002 and the DIRB *Shewanella colwelliana* under simulated Archean ocean conditions (0.5 mM $Fe^{2+}{}_{aq}$, 0.67 mM $SiO_{2\ aq}$) with varying concentrations of PO_4^{3-} (3.67 and 367 μM) and Ni (0.4, 4 and 40 μM). High Ni (4, 40 μM) inhibited growth, except at high PO_4^{3-} (365 μM) with 4 μM Ni, whereas total cell counts temporarily increased from 2×10^7 cells/mL at day 60 to 6×10^7 cells/mL at day 135, followed by a decline to 4×10^7 cells/mL by day 195. Low PO_4^{3-} concentrations (3.67 μM) limited growth except at low Ni (0.4 μM), rising from 2×10^7 cells/mL on day 60 to 8×10^7 cells/mL by day 82. These results suggest that first, the combined stress of high Ni toxicity and low PO_4^{3-} availability likely constrained cyanobacterial proliferation, possibly delaying the onset of the GOE. Second, DIRB could remobilize PO_4^{3-} during Fe(III) reduction, thereby sustaining microbial activity and maintaining iron cycling in the early ocean.

1. Introduction

Banded iron formations (BIF) constitute the worlds' largest iron ore deposits (Beukes, 1973; Trendall, 2002) and occur on nearly every continent (Bekker et al., 2004; Konhauser et al., 2017). Owing to their antiquity and prolonged deposition, BIFs serve as critical archives of ancient seawater chemistry and early microbial life. The earliest primary iron mineral precipitation is attributed to biological activity in the photic zone over continental shelves (see (Konhauser et al., 2017) for review), including anoxygenic photosynthesizers (the so-called photoferrotrophs) that used dissolved Fe(II) (instead of water) as the electron donor for photosynthesis. The Fe(II) oxidation formed Fe(III), which precipitated out of the seawater as a ferric oxyhydroxide such as ferrihydrite, $Fe(OH)_3$ (reaction 1), often with adsorbed silica or forming aggregates composed of Fe(III), Fe(II), and silica (Dreher et al., 2025; Percak-Dennett et al., 2011; Wu et al., 2012). Later, cyanobacteria evolved oxygenic photosynthesis, producing free O_2 from water (reaction 2), which then abiotically oxidized Fe(II) in seawater to form ferrihydrite (reaction 3). The massive deposition of BIF between 2.6 and 2.45 Ga has been attributed to the diversification of cyanobacteria immediately preceding the GOE (Cloud, 1973, Cloud, 1965; Dreher et al., 2026; Li et al., 2024). These Fe(III) minerals subsequently underwent reduction, potentially in deeper anoxic water layers and, ultimately, on the seafloor, mediated by DIRB ((Lovley and Phillips, 1988) (reaction 4)). Li et al., 2017 further proposed that the poorly crystalline Fe(III) (oxyhydr)oxides reacted with Fe(II) from hydrothermal vents (Kump and Barley, 2007), leading to the formation of magnetite. These processes can partially account for the direct formation of minerals like siderite, magnetite or Fe(II)-silicates, which then underwent further diagenesis and transformation into today's BIF minerals like siderite, magnetite hematite or greenalite (Halama et al., 2016; Köhler et al., 2013; Konhauser et al., 2005; Posth et al., 2013).

* Corresponding author.
E-mail addresses: kurtk@ualberta.ca (K.O. Konhauser), andreas.kappler@uni-tuebingen.de (A. Kappler).

https://doi.org/10.1016/j.chemgeo.2026.123499
Received 1 December 2025; Received in revised form 21 April 2026; Accepted 16 May 2026
Available online 21 May 2026

$$4Fe^{2+} + CO_2 + 11H_2O \rightarrow 4Fe(OH)_3 + CH_2O + 8H^+ \quad (R1)$$

$$H_2O + CO_2 \rightarrow O_2 + CH_2O \quad (R2)$$

$$4Fe^{2+} + O_2 + 10H_2O \rightarrow 4Fe(OH)_3 + 8H^+ \quad (R3)$$

$$8H^+ + 4Fe(OH)_3 + C_3H_5O_3^- \rightarrow 4Fe^{2+} + 10H_2O + C_2H_4O_2 + HCO_3^- \quad (R4)$$

Although cyanobacteria likely originated around more than 3.0 billion years ago (Sánchez-Baracaldo et al., 2022), their ecological and biogeochemical impact became more pronounced much later, during the Neoarchean. Recent geochemical evidence—including nitrogen isotopes in BIFs (Liang et al., 2025) and thallium isotopes in shales (Chen et al., 2025)—reveals the presence of dynamic, regionally extensive marine oxygen oases by ~2.65–2.5 billion years ago. These data suggest that oxygenic photosynthesis by cyanobacteria created transient but significant oxygenated environments well before the GOE at 2.45 Ga (Poulton et al., 2021; Sánchez-Baracaldo et al., 2022). The delayed ecological dominance of cyanobacteria likely reflects a combination of factors, including the evolution of filamentous morphologies, limited habitable space (Ozaki et al., 2019), and nutrient availability, with PO_4^{3-} being the most probable limiting factor (Reinhard et al., 2017). However, the exact concentration of PO_4^{3-} in Neoarchean seawater, and whether it was abundant or limiting, remains a matter of debate (Bjerrum and Canfield, 2002; Bruland and Lohan, 2003; Jones et al., 2015; Konhauser et al., 2007; Li et al., 2011; Planavsky et al., 2010). Moreover, it is important to note that under limiting (low) PO_4^{3-} concentrations, it is not only the total concentration, but also the amount of PO_4^{3-} that can be recycled back into solution by DIRB that controls the survival of early bacteria.

Phosphorus (P), alongside with trace metals, played a critical role in regulating early ocean productivity. Bioavailable PO_4^{3-}, essential for ATP generation, nucleic acids and membranes, directly constrains microbial growth; making the reconstruction of ancient seawater PO_4^{3-} concentrations a key objective (Bjerrum and Canfield, 2002; Kipp and Stüeken, 2017). Low P/Fe ratios (<0.1 at ~3.0 Ga) have been used to suggest a 'phosphate crisis', with seawater PO_4^{3-} estimated at 0.15–0.6 μM, which is 10 times lower than modern levels (Bjerrum and Canfield, 2002; Bruland and Lohan, 2003; Rego et al., 2023). However, high dissolved SiO_2 in the Archean oceans likely reduced PO_4^{3-} sorption onto ferrihydrite (Konhauser et al., 2007), potentially allowing concentrations to remain stable or even reach four times modern levels (Planavsky et al., 2010). Competition for sorption sites with organic matter (Li et al., 2011; Sundman et al., 2016; Yan et al., 2016) also further supports elevated PO_4^{3-} availability. Additionally, the co-occurrence of apatite with greenalite in BIFs implies hydrothermal PO_4^{3-} inputs (Rasmussen et al., 2021). Conversely, Mg^{2+} and Ca^{2+} may negate silica's inhibition of PO_4^{3-} sorption, lowering estimates to 0.04–0.13 μM (Jones et al., 2015), approaching the growth limit of *Synechococcus* sp. PCC 7002 (~0.1 μM; (Selão et al., 2019). Overall, it thus remains possible that phosphate was a severely limiting nutrient in the Archean. Sustaining life under such conditions likely required efficient P recycling or microbial release from Fe(III) minerals, with DIRB mobilizing 3–25% of Fe-bound PO_4^{3-} (Roden and Edmonds, 1997). However, it remains to be studied how much PO_4^{3-} DIRB can recycle back into solution during highly dynamic microbial iron cycling, mimicking BIF deposition in the early ocean water column, in comparison to pure minerals. As described in Konhauser et al. (2007), the presence of silica during Fe(II) oxidation can influence the amount of PO_4^{3-} sorbed to or co-precipitated with iron minerals. Similar, as indicated in previous studies (Dreher et al., 2025; Schad et al., 2022) during microbial cycling in the presence of silica, some Fe(II) aggregated with silica, most likely influencing the amount of scavenged PO_4^{3-} during mineral precipitation. One factor that has not been considered in explaining the temporal gap between cyanobacterial evolution and the onset of the GOE is the role of trace metals, particularly Ni. It critically influences nutrient cycling and microbial metabolism in the early ocean, serving as a critical cofactor for enzymes that mediate ureolysis, methanogenesis, hydrogenotrophy, and acetogenesis. In methanogens, Ni-bearing enzymes such as methane hydrogenases and methyl-coenzyme M reductase, the latter containing the distinctive Ni-bearing cofactor F_{430} (Hausinger, 1987), are indispensable. Experimental studies have demonstrated that methanogen growth becomes severely limited at Ni concentrations <200 nM (Kida et al., 2001; Schönheit et al., 1979). Coupled with geochemical evidence of elevated pre-GOE Ni availability, these findings support the hypothesis that vigorous methanogenesis sustained high atmospheric methane (CH_4), consuming free O_2 and delaying the onset of the GOE (Konhauser et al., 2009; Eickhoff et al., 2014; Robbins et al., 2016). Interestingly, cyanobacteria also exhibit variable Ni requirements and tolerances: *Synechococcus* sp. PCC 7002 requires ~5 μM Ni for effective urea utilization (Sakamoto and Bryant, 2001), *Anabaena doliolum* tolerates up to 10 μM Ni (Shukla et al., 2009), whereas *Anacystis nidulans* and *Spirulina platensis* are capable of growth at much lower concentrations, down to ~1.7 μM Ni (Azeez and Banerjee, 1991).

The influence of microbial Fe cycling by cyanobacteria and DIRB on the fate of Ni and P under Archean-like conditions remains unconstrained. It also remains unclear how the microorganisms implicated in BIF deposition responded to elevated Ni but low P concentrations. This study investigates how microbial abundance (cell density) and activity (O_2 production by cyanobacteria and Fe(III) reduction by DIRB) were affected under these conditions. To address this, we conducted controlled microcosm experiments co-culturing the cyanobacterium *Synechococcus* sp. PCC 7002 with the DIRB *Shewanella colwelliana*. Simulating early ocean geochemistry, the experiments contained 0.5 mM Fe(II) and 0.67 mM SiO_2, with variable Ni concentrations (0.4, 4, and 40 μM) and PO_4^{3-} concentrations (3.67 μM and 367 μM). We monitored cell density, dissolved O_2, total and dissolved Fe(II), total Fe, as well as dissolved SiO_2, PO_4^{3-}, and Ni concentrations over successive redox cycles.

2. Material and methods

2.1. Cultivation of microorganisms and growth conditions

The cyanobacterium *Synechococcus* sp. PCC 7002, obtained from Gen Enomoto (University of Freiburg), was cultivated in oxic A+ medium, prepared from five stock solutions. Stock 1 (1:2 dilution) contained 3.89 g $FeCl_3 \cdot 6H_2O$, 34.3 g H_3BO_3, 4.3 g $MgCl_2 \cdot 4H_2O$, 0.315 g $ZnCl_2$, 0.03 g MoO_3, 0.003 g $CuSO_4 \cdot 5H_2O$, and 0.0122 g $CoCl_2 \cdot 6H_2O$ in Milli-Q water (1 L total). Stock 2 consisted of 100 g Trizma base adjusted to pH 8.2 with HCl and diluted to 1 L with Milli-Q water. Stock 3 included 0.5 g KH_2PO_4, 10 g $NaNO_3$, 24.4 g $MgSO_4$, 180 g NaCl, and 6 g KCl in 1 L Milli-Q water. Stock 4 contained 0.3 g Na_2EDTA in 100 mL Milli-Q water, and stock 5 contained 2.8 g $CaCl_2$ in 100 mL Milli-Q water. To prepare 1 L of A+ medium, 4 mL of stock 1, 20 mL of stock 2, 200 mL of stock 3, and 4 mL each of stocks 4 and 5 were combined and diluted to volume with Milli-Q water. Cultures were grown at 25 °C in Erlenmeyer flasks on a shaker (60 rpm) for aeration and CO_2 exchange, under a 40-watt halogen bulb providing 300–500 lx on an 18/6 h light–dark cycle. Cultures were maintained until reaching a cell density of ~10^8 cells/mL.

The DIRB *Shewanella colwelliana*, obtained from the German Collection of Microorganisms and Cell Cultures (DSMZ), was cultivated on DSM 514 agar plates. The medium was prepared using premixed Bacto™ Marine Broth (DIFCO 2216) and included 15 g/L agar, 5 g/L Bacto™ peptone, 1 g/L Bacto™ yeast extract, and 0.1 g/L Fe(III) citrate, along with a defined seawater salt mixture: 19.45 g/L NaCl, 5.90 g/L $MgCl_2$, 3.24 g/L Na_2SO_4, 1.80 g/L $CaCl_2$, 0.55 g/L KCl, 0.16 g/L $NaHCO_3$, 0.08 g/L KBr, 0.34 g/L $SrCl_2$, 22 mg/L H_3BO_3, 0.04 g/L sodium silicate, 0.024 g/L NaF, 1.60 g/L $(NH_4)NO_3$, and 8 mg/L Na_2HPO_4. The pH was adjusted to 7.14 using HCl prior to autoclaving. Cultures were incubated at 25 °C to promote bacterial growth. Co-culturing *S. colwelliana* with *Synechococcus* sp. PCC 7002 enabled simulation of microbial

interactions under redox cycling. The rationale for including *S. colwelliana* lies in its metabolic versatility: it can utilize oxygen when available and switch to fermentation or dissimilatory Fe(III) reduction under anoxic conditions, as would have occurred in the lower water column of Archean ferruginous oceans.

2.2. Setup of iron cycling experiments

We co-cultivated the planktonic cyanobacterium *Synechococcus* sp. PCC 7002 and the Fe(III)-reducing bacterium *Shewanella colwelliana* in anoxic artificial seawater (ASW) medium containing 500 μM dissolved Fe^{2+} and 670 μM monomeric silica. Two phosphate regimes were used: a 'high-phosphate' condition (367 μM, between 0.3 and 60 μM left in solution after first Fe(II) oxidation period) and a 'low-phosphate' condition (3.67 μM, between 0.3 and 4 μM left in solution after the first Fe (II) oxidation period, none left in solution after the second Fe(II) oxidation period). The high-phosphate ASW was prepared using Milli-Q water and the following salt composition: 17.3 g/L NaCl, 8.6 g/L $MgCl_2{\cdot}6H_2O$, 0.025 g/L $MgSO_4{\cdot}7H_2O$, 0.99 g/L $CaCl_2{\cdot}2H_2O$, 0.39 g/L KCl, 0.059 g/L KBr, 0.05 g/L KH_2PO_4, 0.25 g/L NH_4Cl, and 2 g/L $NaHCO_3$. For the low-phosphate condition, KH_2PO_4 was reduced to 0.5 mg/L (3.67 μM).

All salts, the bicarbonate buffer (30 mM), and the monomeric silica stock solution ($Na_2O_3Si{\cdot}9H_2O$) were purged with N_2 (or N_2/CO_2 at a 90:10 ratio for the buffer) and autoclaved separately to maintain anoxic conditions. The ASW medium was autoclaved in a Widdel flask and cooled to room temperature (~20 °C) before sterile addition of the bicarbonate buffer and silica stock. The pH was adjusted to 7.0 using 1 M anoxic HCl under sterile conditions while maintaining an anoxic headspace. Vitamin and trace element solutions were then added to the filtered medium, and the pH was readjusted if necessary.

The prepared medium was dispensed in 100 mL aliquots into sterile 250 mL Schott bottles under a continuous stream of N_2/CO_2 gas. Dissolved O_2 concentrations were monitored throughout the experiments, and any bottles exceeding 3 μM O_2 were flushed with N_2/CO_2 to restore anoxia. Nickel was added from an anoxic, sterile $NiCl_2$ stock solution to final concentrations of 0.4, 4, or 40 μM Ni. The rationale for choosing these Ni concentrations is provided in the SI file.

To initiate Fe cycling experiments, an anoxic, sterile $FeCl_2$ x 4 H_2O stock solution (100 mM or 1 M) was aseptically added to each bottle. The pH remained circumneutral (7.0 ± 0.05) after Fe(II) addition and remained between 7.0 and 7.5 throughout the experiment. Bottles were then subjected to alternating light and dark conditions to simulate two full redox cycles, promoting microbial Fe(II) oxidation during light phases and Fe(III) reduction during dark phases. All experiments were conducted in triplicates.

PCC 7002 stock cultures were washed three times with artificial seawater (ASW) and inoculated into Schott bottles to achieve a final cell density of 10^6 cells/mL. Following the termination of the first oxidation half-cycle, the bottles were wrapped in aluminum foil to inhibit photosynthetic activity and purged with a 10/90 N_2/CO_2 mixture until dissolved oxygen concentrations dropped below 3 μM. Separately, cultured *S. colwelliana* cells were suspended, washed three times with ASW, and introduced into the system to the same final cell density (10^6 cells/mL). To initiate Fe(III) reduction, sodium lactate ($NaC_3H_5O_3$) was added as an electron donor and carbon source, with its concentration aimed to achieve 70% Fe(III) reduction (Konhauser et al., 2005). Once this reduction threshold was reached, the bottles were unwrapped and re-exposed to light to reactivate photosynthesis.

2.3. Quantification of Fe redox species using the spectrophotometric Ferrozine assay

We followed the protocol of Hegler et al. (2008) to quantify Fe^{2+} concentrations via spectrophotometry. For Fe^{2+} analysis, samples were dissolved and diluted in 1 M HCl to ensure iron concentrations ≤1 mM. In a 96-well plate, 80 μL of 1 M HCl was combined with 20 μL of sample, followed by a 15-min incubation to stabilize the solution. Next, 100 μL of ferrozine reagent was added, forming a light-sensitive purple complex with Fe^{2+} that absorbs at 562 nm. After a 5-min complexation period in the dark, absorbance was measured using a Multiskan™ GO Microplate Spectrophotometer (Thermo Fisher Scientific, USA).

For total iron ($Fe_{(tot)}$) quantification, the protocol was adjusted: 1 M HCl was replaced with 80 μL of 10% (*v*/v) hydroxylammonium hydrochloride (HAHCl) to reduce Fe^{3+} to Fe^{2+}. This step required a 30-min incubation to ensure complete reduction before adding ferrozine. To prevent photodegradation, both ferrozine and HAHCl solutions were stored and handled in the dark. Calibration was performed using iron standards (0–1000 μM) to generate a standard curve for concentration calculations.

2.4. Quantification of dissolved silica using the Molybdenum Blue method

Dissolved silica, including monomeric silica and colloidal silicic acid (Si-Si-colloids), was quantified using the Molybdenum Blue method (Fanning and Pilson, 1973). Samples were first filtered through 0.22 μm PES membranes and diluted with Milli-Q water to a final volume of 1 mL. To initiate the reaction, 40 μL of ammonium heptamolybdate tetrahydrate solution (prepared by dissolving 6.33 g in 50 mL of 4.5 M H_2SO_4) was added, forming a blue silica-molybdate complex within 15 min incubation time. To eliminate phosphate interference, 40 μL of oxalic acid dihydrate (10 g/100 mL Milli-Q water) was introduced. Finally, 20 μL of ascorbic acid was added as a reducing agent to stabilize the complex. After 30–60 min of incubation in the dark, absorbance was measured at 810 nm using a spectrophotometer. Measured values were calibrated against a calibration curve consisting of silica standards (1–100 μM).

2.5. Oxygen quantification by optode sensors

Dissolved O_2 was quantified using a luminophore optode foil from PreSens (Regensburg, Germany), which operates based on dynamic luminescence quenching. Small 3 × 3 mm pieces of foil were affixed with silicone glue within the lower 2 cm of experimental bottles to ensure direct contact with the liquid phase. The interaction between the optode foil (luminophore) and oxygen molecules (quencher) results in an energy transfer that reduces the luminescence signal of the foil. Oxygen concentration in the liquid phase was calculated using the Stern-Volmer equation, which relates luminescence intensity to oxygen levels. To account for temperature variations, a temperature sensor was placed in a co-incubated Schott bottle under identical experimental conditions. Each bottle and optode foil setup underwent a fresh two-point calibration before measurements. The calibration included one point at full O_2 saturation and another under oxygen-free conditions. For the first calibration point, 100 mL of pure artificial seawater (ASW) was added to a 250 mL Schott bottle containing the optode foil and stirred vigorously until complete O_2 saturation was achieved. For the second calibration point, 10% *w/v* sodium dithionite ($Na_2S_2O_4$) was added to the same bottle to eliminate all remaining dissolved oxygen, creating an oxygen-free environment.

2.6. ICP-MS measurements of Ni and P

Dissolved Ni and P were quantified using an Agilent 7900 ICP-MS (Santa Clara, USA) with a helium flow of 1–3 mL/min. Ni and P single element standards (1000 μg/L) from Agilent Technologies were combined and diluted in ASW matrix to serve as 10 standards ranging from 0.05 to 1000 ppb. Internal rhodium standards were used for corrections of instrumental shifts. The samples were filtered with 0.22 μM PES filters, diluted in 1% HCl and stored at 4 °C until measurement.

2.7. Cell counts by hemocytometry

Cell density was determined using a Leica CTR 5500 microscope and a Neubauer-improved hemocytometer by Hirschmann (Eberstadt, Germany). A 10 μL sample was pipetted between the sample holder and coverslip of the hemocytometer. At 400× magnification, cells were counted within the smallest grid squares until a total of 100 cells was reached. The cell count per small square was then multiplied by the dilution factor and a volume factor of 2.5×10^7 to calculate the actual cell density in cells/mL. Theoretically, the cyanobacteria used can be differentiated from the DIRB based on their morphology, size, and autofluorescence. Additionally, cyanobacteria displayed natural autofluorescence, which facilitated their identification under the microscope. However, due to toxicity effects occurring over the course of the experiments changing the cell morphology, we were unable to visually distinguish both cell types. We, therefore, only provide absolute cell numbers.

2.8. Mineral analysis by μ-X-ray diffraction (μXRD)

The methodology for μXRD can be found in the supporting information.

3. Results

We conducted microbial iron cycling experiments using 0.5 mM dissolved Fe^{2+} and 0.67 mM SiO_2, under varying PO_4^{3-} and Ni concentrations. Phosphate was adjusted to either low (3.67 μM) or high (367 μM) levels, while Ni was varied across low (0.4 μM), medium (4 μM), and high (40 μM) treatments. Throughout the experiments, we monitored bacterial growth, metabolic activity, and the distribution of dissolved Ni and PO_4^{3-}. Differences in microbial growth became apparent during the second oxidation period, as reflected by distinct colour changes in the cultures: green indicated dense, healthy cyanobacterial growth, whereas orange signaled Fe(III) (oxyhydr)oxide precipitation and reduced biomass. Two clear trends emerged—higher PO_4^{3-} and/or lower Ni concentrations promoted greener, more robust cultures (Fig. 1).

3.1. Low phosphate scenarios

Under low PO_4^{3-} conditions, cell growth showed distinct responses across the different Ni concentrations (Fig. 2A). In the 'low Ni' setup, cell densities remained unchanged during the initial oxidation period, then increased from 2×10^7 to 6×10^7 cells/mL following the second oxidation phase and subsequently plateaued during the reduction period. In contrast, no detectable cell growth occurred in either the 'medium Ni' or 'high Ni' setups throughout the entire experiment.

Dissolved O_2 measurements (Fig. 2B) revealed distinct trends across Ni treatments. In the 'low Ni' setup, O_2 concentrations rose to 80 μM during the first oxidation period and further increased to 150 μM during the second. In contrast, the 'medium Ni' setup accumulated more O_2 (250 μM) in the first oxidation phase but only 20 μM in the second. No free O_2 was detected at any point in the 'high Ni' setup. The production of O_2 led to the abiotic oxidation of Fe(II) to Fe(III), followed by microbial re-reduction of Fe(III) to Fe(II) during the dark (reducing) periods (Fig. 2F). Throughout the experiment, total dissolved Fe concentrations remained stable across all setups, ranging between 400 and 500 μM.

The behavior of dissolved Fe^{2+} (Fig. 2D) is particularly informative for understanding the subsequent dynamics of Ni and PO_4^{3-}. During the first oxidation period (days 0–8), Fe^{2+} was completely removed in all treatments due to oxidation. Thereafter, Fe redox cycling became strongly dependant on Ni concentrations. In the 'low Ni' setup, 200 μM Fe^{2+} accumulated during the first dark period, was fully re-oxidized during the second oxidation phase, and partially re-reduced (120 μM Fe^{2+}) during the second dark period. The 'medium Ni' setup showed more limited reduction, with 80 μM Fe^{2+} generated in the first dark phase, followed by complete oxidation and no additional reduction thereafter. In the 'high Ni' setup, 100 μM Fe^{2+} was produced during the first reduction period and remained unchanged, with no further redox cycling during the second Fe cycle (days 76–195).

Dissolved SiO_2 concentrations declined from 600 to 500 μM during the first oxidation period across all experimental setups (Fig. 2C). Levels remained stable at 500 μM during the first reduction phase, then rose to 550 μM during the second oxidation period (days 76–82). Silica continued to increase during the subsequent reduction phase (days 82–195), reaching initial values of 600 μM by the end of the experiment.

In the 'low Ni' setup, dissolved Ni remained consistently at or below the limit of quantification (0.04 μM; Fig. 2G). In the 'medium Ni' treatment, Ni concentrations stayed steady at approximately 1 μM throughout the experiment. In contrast, the 'high Ni' setup showed pronounced fluctuations: dissolved Ni decreased from 14 to 10 μM during the first oxidation period, increased to 13 μM during the subsequent reduction phase, decreased again to 8 μM during the second oxidation period, and then stabilized at that level.

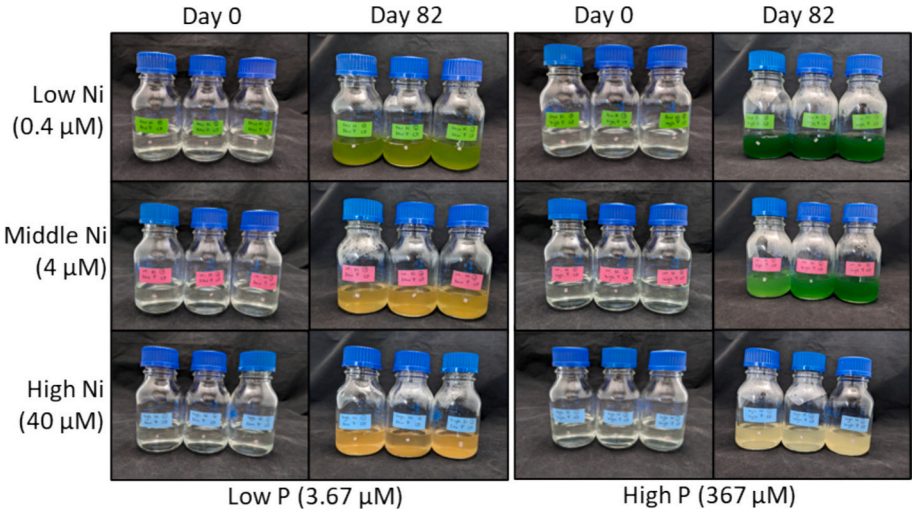

Fig. 1. Photos of experimental bottles after 0 days and 82 days (second oxidation period). The bottles contain cyanobacteria (green colored), *Shewanella* (colorless), Fe(III) (oxyhydr)oxide minerals (orange colored) and SiO_2 (colorless or white colored). (For interpretation of the references to colour in this figure legend, the reader is referred to the web version of this article.)

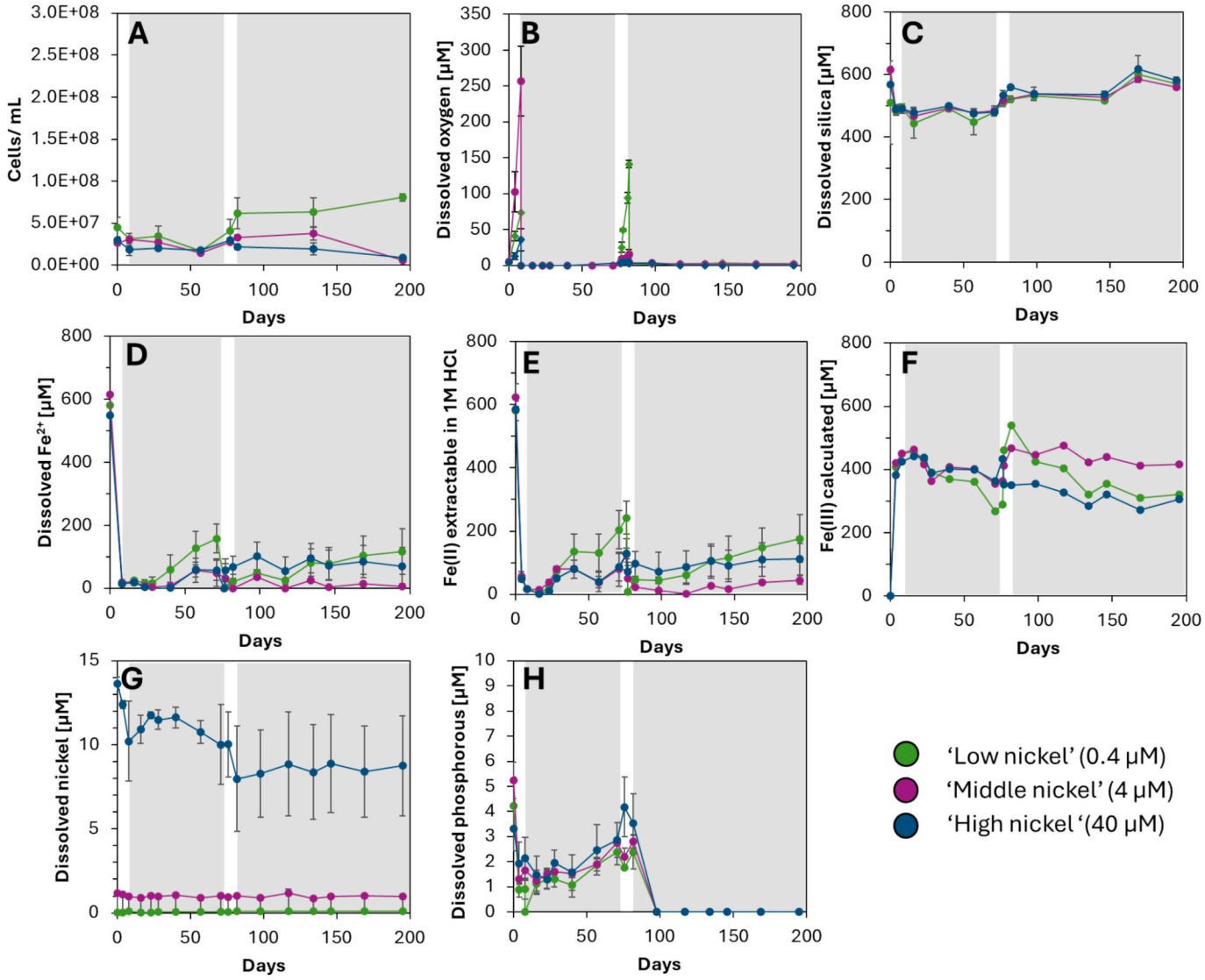

Fig. 2. Geochemical data of the 'low phosphate' experiments containing 0.4 µM Ni ('low nickel') shown in green, 4 µM Ni ('medium Ni') shown in purple, and 40 µM Ni ('high Ni') shown in blue. Cell numbers (sum) of *Synechococcus* sp. PCC 7002 and *S. colwelliana* (A), dissolved O_2 (B), dissolved SiO_2 (C), dissolved Fe^{2+} (D), total Fe(II) (E), Fe(III) calculated as difference from the mean values of the 1 M HCl extractable total Fe and Fe(II)(F), dissolved Ni (G), and dissolved PO_4^{3-} (H). All data is presented as mean of triplicates ± standard deviation. Grey shaded areas mark microbial Fe(III) reduction in dark while light areas mark times of active O_2 production in light. (For interpretation of the references to colour in this figure legend, the reader is referred to the web version of this article.)

Dissolved PO_4^{3-} concentrations across all setups initially ranged from 4 to 6 µM, decreased to 0.5–2 µM during the first oxidation period, and rose again to 2–4 µM just before the second oxidation phase (Fig. 2H). However, during the second reduction phase (days 82–195), PO_4^{3-} was completely removed from solution, with concentrations falling below the detection limit (0.02 µM).

3.2. High phosphate scenario

Cell growth, dissolved O_2, and key chemical species were monitored throughout the experiment across all three Ni treatments. In the 'low Ni' setup, no cell growth was observed initially despite detectable metabolic activity (Fig. 3A). However, by day 195—immediately prior to the second oxidation period—cell density increased from 2×10^7 to 8×10^7 cells/mL. In the 'medium Ni' setup, growth was only detected during the second oxidation phase, reaching a maximum of 5×10^7 cells/mL. No detectable cell growth occurred in the 'high Ni' setup at any point during the experiment.

Dissolved O_2 followed a similar trend, with concentrations decreasing as Ni increased (Fig. 3B). The 'low Ni' setup accumulated ~100 µM O_2 during the first oxidation period and ~ 350 µM during the second. In the 'medium Ni' treatment, O_2 accumulation was limited to ~150 µM during the second oxidation phase. No free O_2 was detected in the 'high Ni' setup.

The calculated Fe(III) concentrations remained comparable across all setups, increasing from 0 µM to then ranging between 400 and 600 µM (Fig. 3F). Total Fe(II) broadly mirrored the trends in dissolved Fe^{2+} (Fig. 3E). In the 'low Ni' setup, Fe^{2+} reached 200 µM at the end of both reduction phases. In the 'medium Ni' treatment, Fe^{2+} peaked at 150 µM before the second oxidation and decreased to 100 µM by its end. In the 'high Ni' setup, Fe^{2+} concentrations reached 160 µM by day 70 and 200 µM by day 150. All setups exhibited complete Fe^{2+} oxidation during the first oxidation period (Fig. 3D). In the 'low Ni' setup, Fe(III) was reduced to ~80 µM Fe^{2+} by day 76 and further to ~100 µM by the end of the experiment. The 'medium Ni' setup showed more limited reduction, with ~50 µM Fe^{2+} by day 70 and 20 µM by day 195. In the 'high Ni' setup, 100 µM Fe^{2+} was generated by day 100, with no evidence of subsequent re-oxidation.

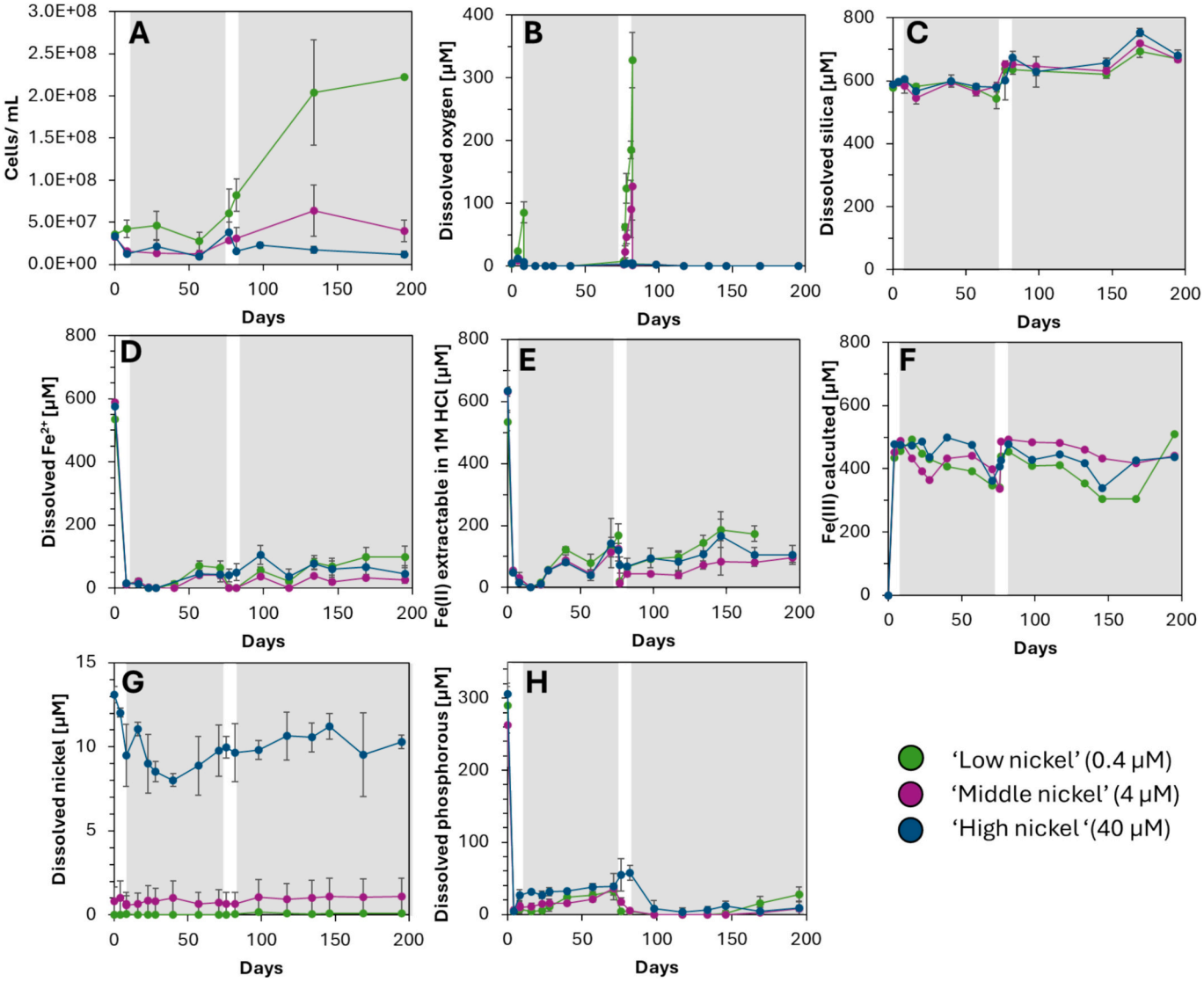

Fig. 3. Geochemical data of the 'high phosphate' experiments containing 0.4 µM Ni ('low nickel') in green, 4 µM Ni ('medium Ni') in purple, 40 µM Ni ('high Ni') in blue. Cell counts of *Synechococcus* sp. PCC 7002 and *S. colwelliana* (A), dissolved O_2 concentrations (B), dissolved SiO_2 (C), dissolved Fe^{2+} (D), total Fe(II) (E), Fe(III) calculated as difference from the mean values of the 1 M HCl extractable total Fe and Fe(II) (F), dissolved Ni (G), and dissolved PO_4^{3-} (H). All data is presented as mean of triplicates ± standard deviation. Grey shaded areas mark microbial Fe(III) reduction in dark while light areas mark times of active O_2 production in light. (For interpretation of the references to colour in this figure legend, the reader is referred to the web version of this article.)

Dissolved SiO_2 remained stable at ~600 µM across all setups until the second reduction phase, during which it increased to 700 µM and remained constant thereafter (Fig. 3C).

In the 'low Ni' setup, dissolved Ni remained below the detection limit throughout the experiment (Fig. 3G). In the 'medium Ni' setup, Ni concentrations remained stable at approximately 2 µM. In the 'high Ni' setup, concentrations began at 13 µM, declined to 10 µM during the first oxidation phase (days 0–8), further decreased to 8 µM by day 50 during the reduction phase, and then stabilized around 10 µM for the remainder of the experiment.

Phosphate dynamics followed a similar pattern across all setups (Fig. 3H). Starting at approximately 300 µM, PO_4^{3-} was fully removed from solution during the first oxidation period. During the subsequent reduction phase, PO_4^{3-} was partially remobilized, with concentrations reaching ~30 µM in the 'low Ni' and 'medium Ni' setups and ~ 60 µM in the 'high Ni' setup. This was followed by complete re-precipitation during the second oxidation phase. Only the 'low Ni' setup showed an additional release of PO_4^{3-} (~40 µM) by the end of the experiment.

4. Discussion

Our results suggest that high Ni concentrations (added 4 and 40 µM, with 1 µM to 8–14 µM in solution, respectively) combined with low PO_4^{3-} availability (3.67 µM, with 0–4 µM in solution) would have posed a significant constraint on bacterial growth in early oceans, affecting both cyanobacteria (*Synechococcus* sp. PCC 7002) and DIRB (*Shewanella colwelliana*). Two key findings emerged. First, under geochemical conditions realistic for ancient oceans—characterized by low PO_4^{3-} (3.67 µM) and low total Ni (0.4 µM, with ~0.2 µM in solution)—bacterial growth was limited. Second, the toxic effects of the lowest Ni concentrations (0.4 µM) were mitigated when PO_4^{3-} concentrations were high (367 µM, with 0–60 µM in solution), highlighting the protective role of phosphorus under metal stress conditions.

4.1. Nickel dynamics

Nickel is a well-known bacterial toxicant at elevated concentrations, primarily due to its ability to substitute for essential metals in

metalloproteins, thereby disrupting their function (Macomber and Hausinger, 2011). This effect is particularly significant in cyanobacteria such as *Synechococcus* sp. PCC 7002, where metalloproteins are central to both photosynthesis and nutrient metabolism. For example, ferredoxin-$NADP^+$ oxidoreductase—a key enzyme in the photosynthetic electron transport chain—relies on precise metal coordination for proper function (Schluchter and Bryant, 1992), while other metalloproteins are involved in cobalamin transport (Pérez et al., 2016). Similarly, in *Shewanella* species, metalloproteins are critical for Fe acquisition and Fe(III) reduction (Trindade et al., 2024).

Ni toxicity extends beyond disruption of metalloproteins; it can also bind to the catalytic sites of non-metalloproteins, inhibiting their function (Macomber and Hausinger, 2011). In addition, Ni interactions with cellular biomolecules can induce oxidative stress (Huang et al., 2021; Macomber and Hausinger, 2011). Although oxidative stress is often cited as a key mechanism of Ni toxicity, recent studies suggest its role may be overstated, as Ni can impair microbial physiology even under anoxic conditions (Macomber and Hausinger, 2011).

The impact of Ni on cyanobacterial growth is highly concentration-dependent, with both deficiency and excess leading to adverse effects. For instance, *Spirulina platensis* exhibited reduced growth at Ni concentrations as low as 0.1 μM (Azeez and Banerjee, 1991), while *Anabaena doliolum* tolerated up to 10 μM before exhibiting toxic effects (Shukla et al., 2009). *Synechococcus* sp. PCC 7002 requires at least 5 μM Ni for optimal growth with urea as N-source (Sakamoto and Bryant, 2001), highlighting the considerable species-specific variation in Ni requirements and tolerance among cyanobacteria. In contrast, *Shewanella* species display significantly higher Ni tolerance. For example, *S. oneidensis* can withstand Ni concentrations up to 100 μM before showing signs of toxicity (Buchman et al., 2020). This elevated tolerance is attributed to efficient detoxification mechanisms such as complexation by chelating agents, like EDTA, or binding to the surface of bacterial cell walls, as shown for cadmium in Flynn et al. (2014), mitigation of oxidative stress via catalase and superoxide dismutase (Abuladze et al., 2023), and specialized efflux systems, such as RcnA and NreB, which actively export Ni from the cell and are widespread among prokaryotes (Macomber and Hausinger, 2011).

Our experimental data revealed that dissolved Ni concentrations were consistently lower than expected based on the initial dosing. In the 'low Ni' setup, only 0.04 μM dissolved Ni was measured on day 0, despite an initial addition of 0.4 μM. In the 'medium Ni' and 'high Ni' setups, initially dosed with 4 μM and 40 μM Ni, measured dissolved Ni was 1 μM and 14 μM, respectively. This indicates that approximately 3 μM and 26 μM of Ni were removed from solution, likely through a combination of bacterial uptake, adsorption to the glass bottle walls, and association with solid phases, primarily Fe- and Si-containing minerals. Initial measurements (day 0) prior to Fe^{2+} oxidation confirmed the presence of 500–600 μM Fe^{2+}, 600 μM dissolved SiO_2, standard medium salts, and approximately 5×10^7 cyanobacterial cells/ml, with no detectable Fe(III) or O_2. In the 'high P' setup, ~300 μM dissolved PO_4^{3-} remained in solution, indicating that 70 μM had been precipitated or adsorbed. This raises questions about Ni removal mechanisms. Nickel can form various complexes in seawater with chloride (Niu et al., 2026), carbonate (Hunter et al., 2016), and phosphate (Han et al., 2025), all influencing solubility and mobility.

Microbial cells can also represent a significant sink for Ni in our system. The cyanobacterium *Anacystis nidulans* has been shown to efficiently adsorb Ni, with adsorption efficiency peaking near pH 8. Although our experiments were conducted at pH 7, surface functional groups on the cells remain capable of binding Ni^{2+} (Awasthi and Chand Rai, 2004; Wang and Wood, 1984). Despite Ni's potential toxicity, this adsorption ability highlights a complex interplay between cellular metal demand, environmental conditions, and toxicity thresholds (Azeez and Banerjee, 1991; Nohomovich et al., 2013). Bishop et al. (2019) performed adsorption experiments at pH 8 using *Synechococcus* sp. PCC 7002 at a density of 10^5 cells/mL and measured 63 μmol of Ni adsorbed in a 10 mL setup. Scaling this to our experiments with 5×10^7 cells/mL, and ignoring the pH difference, this corresponds to a theoretical Ni adsorption capacity of approximately 0.0315 mol/L Ni. Since the Ni concentrations we added ranged from 0.4 to 40 μM, this suggests that all Ni added in our experiments could theoretically be adsorbed onto cells.

Dissolved Ni concentrations remained stable in the 'low Ni' and 'medium Ni' setups throughout the experiment, whereas the 'high Ni' setup showed progressive Ni removal associated with repeated Fe(II) oxidation and Fe(III) (oxyhydr)oxide precipitation. Specifically, in the 'low P' treatment, up to 6 μM of Ni was removed from solution by day 87, following the second oxidation period, while in the 'high P' treatment, up to 5 μM Ni was lost by day 40, during the first reduction phase, highlighting the influence of both redox cycling and PO_4^{3-} availability on Ni partitioning.

In the 'high P' experimental setup, the transient formation of vivianite ($Fe_3(PO_4)_2{\cdot}8H_2O$) or poorly crystalline Fe(II)-phosphate minerals likely explains the observed PO_4^{3-} removal and may also have acted as a Ni sink via co-precipitation or sorption. Optimal Ni adsorption onto vivianite occurs within a pH range of 6–8, consistent with the experimental pH (~7). At lower pH, competition with protons reduces Ni uptake, while at higher pH, fewer reactive surface sites limit adsorption capacity (Vakili et al., 2021). Although μXRD analyses (see Fig. S1) did not detect crystalline vivianite at the end of the experiments, it is plausible that vivianite (or a poorly crystalline or even amorphous type of Fe(II)-phosphate mineral) formed immediately following Fe(II) addition to the PO_4^{3-}-containing system.

As the experiments progressed, Fe(III) minerals formed during Fe(II) oxidation. Although most Fe(II) was oxidized during the first and second oxidation phases, subsequent Fe(III) reduction was incomplete, leaving Fe(III) (oxyhydr)oxide minerals present throughout the experiment. Nickel interacts with Fe(III) minerals due to similar ionic radius and charge, competing for binding sites in both minerals (Eickhoff et al., 2014; Pantke et al., 2012; Xu et al., 2007) and biomolecules (Zambelli et al., 2011). Previous studies have demonstrated that in the presence of both Fe(III) (oxyhydr)oxides and bacterial cells, Ni preferentially adsorbs to Fe(III)-bearing minerals rather than to the cells themselves, irrespective of SiO_2 presence (Eickhoff et al., 2014). This suggests that in Archean-like oceans, microbial precipitation of Fe(III) (oxyhydr)oxides—particularly ferrihydrite-like phases—would have effectively scavenged much of the dissolved Ni from seawater.

4.2. Phosphorus Dynamics

Multiple studies have been discussing the early ocean seawater concentrations of PO_4^{3-} ranging from severely limiting 0.15 μM (Bjerrum and Canfield, 2002) to concentrations similar to modern oceans (Konhauser et al., 2007). Here, we focus on the impact of limiting PO_4^{3-} concentrations on bacterial survival and iron cycling. The minimum PO_4^{3-} requirement for *Synechococcus* sp. PCC 7002 has not yet been established. However, other *Synechococcus* species have been shown to survive at PO_4^{3-} concentrations as low as 50 nM (Scanlan et al., 1997), and in extreme cases, even at 3 nM (Kretz et al., 2015). These findings support our observation that the 'low P' concentration of 3.67 μM in our experimental system was not growth-limiting for *Synechococcus* sp. PCC 7002. Nevertheless, growth was slower under low PO_4^{3-} conditions, with cultures reaching approximately 8×10^7 cells/mL after 195 days, compared to 2×10^8 cells/mL in the 'high P' setup over the same period.

Phosphate dynamics in our system were closely tied to Fe redox cycling. During Fe(III) reduction in the 'low P' setups, we observed remobilization into solution of up to 4 μM PO_4^{3-}. In the 'high P' setups, phosphate remobilization was substantially greater, reaching up to 30 μM in the 'low' and 'medium Ni' experiments, and up to 60 μM in the 'high Ni' treatment. These findings suggest that a significant fraction of PO_4^{3-} was initially co-precipitated with or adsorbed onto Fe(III) (oxyhydr)oxides, consistent with previous observations by Hemmingsson et al. (2018). Our μXRD analyses (Fig. S1) indicate that all Fe minerals

remained poorly crystalline throughout the experiment, pointing to ferrihydrite-like phases as the predominant Fe(III) mineral. We further hypothesize that some PO_4^{3-} precipitated prior to Fe(II) oxidation may have been associated with Fe(II), possibly as poorly crystalline vivianite or vivianite-like Fe(II)-phosphate phases.

We further observed that Ni toxicity in the 'medium Ni' setups was significantly more pronounced under 'low P' conditions, as indicated by lower dissolved O_2 accumulation (20 μM during the second oxidation (at day 82) and reduced cell density (8×10^7 cells/mL) compared to the 'high P' condition (130 μM O_2, 2.5×10^8 cells/mL). These data suggest a protective, or 'rescue', effect of PO_4^{3-} against Ni toxicity. Such a protective role aligns with previous findings showing that cyanobacteria like *Anabaena variabilis* benefit from PO_4^{3-} availability when recovering from arsenic toxicity (Thiel, 1988). Moreover, multiple studies have demonstrated that elevated PO_4^{3-} concentrations enhance microbial growth rates, implying that it may mitigate metal toxicity indirectly by promoting faster cell growth rather than via a direct detoxification mechanism (Kuffner and Paul, 2001; Lehtimaki et al., 1997; Sabour et al., 2009). The critical role of PO_4^{3-} in modulating metal toxicity is further supported by evidence from cyanobacteria showing that PO_4^{3-} availability positively influenced the expression of metal transporters and detoxification pathways (Huertas et al., 2014).

4.3. The role of Ni and P in the Precambrian Ocean

Estimates for early Earth seawater PO_4^{3-} concentrations suggest levels as low as 0.15–0.6 μM (Bjerrum and Canfield, 2002), although other studies propose that PO_4^{3-} could have been higher than present-day values (Konhauser et al., 2007). Our experiments demonstrate that, in the presence of 'low Ni' (~0.06 μM dissolved Ni), bacterial growth was sustained, however limited, even at dissolved PO_4^{3-} concentrations between 0.1 and 1.2 μM, with cell densities increasing from 4×10^7 to 8×10^7 cells/mL. This implies that any increase in PO_4^{3-} availability in the early ocean would have further enhanced bacterial proliferation. However, dissolved Ni likely imposed significant constraints on early microbial life. Estimates of dissolved Ni concentrations in ancient seawater range from 40 to 400 nM (0.04–0.4 μM) (Eickhoff et al., 2014; Konhauser et al., 2009). Our data show that bacterial growth can occur around 0.1 μM dissolved Ni, even under 'low P' conditions (4 μM total P added, $\leq$ 4 μM in solution). Elevated Ni concentrations, however, are also known to favor methanogenic bacteria (Konhauser et al., 2015; Konhauser et al., 2009), potentially intensifying competition for nutrients and altering ocean-atmosphere chemistry through methane and oxygen cycling.

We observed that in the low P setup, the majority of PO_4^{3-} (80% after the first oxidation step, 100% after the second cycle) was scavenged by the Fe(III) minerals produced by Fe(II) oxidation driven by cyanobacterial O_2 production. However, during Fe(III) reduction by DIRB, up to 100% of the PO_4^{3-} was re-mobilized in the first reduction cycle in the low P setup. In contrast, during the second reduction period—when more crystalline and less reducible Fe(III) minerals had formed—all PO_4^{3-} remained bound in the solid phase. These results highlight the critical importance of DIRB in the Archean water column: PO_4^{3-} initially bound to poorly crystalline Fe(III) BIF precursor minerals could be efficiently re-mobilized by DIRB, a process that was especially crucial given the potential for low estimated PO_4^{3-} concentrations of the early ocean. The re-mobilized PO_4^{3-} in solution therefore was most likely one of the main reasons for the observed bacterial growth in the presence of 0.4 μM Ni.

Our results suggest that low PO_4^{3-} availability (~4 μM) was a key factor constraining cyanobacterial expansion prior to the GOE. While cyanobacteria tolerated dissolved Ni concentrations up to 0.2 μM, with the tolerance facilitated by effective PO_4^{3-} re-mobilization by DIRB, exposure to 1 μM Ni led to strongly reduced cell densities and lower metabolic activity. Even though the typical average ranges for Ni seawater concentrations are stated as 0.04–0.4 μM the early ocean, bacteria might encounter elevated Ni concentrations in upwelling areas or in zones with effective Fe(III) reduction where, Ni is cycled back into the seawater. Thus, with a low PO_4^{3-} concentrations in the seawater, Ni toxicity may have posed a critical barrier to the proliferation of oxygenic phototrophs at concentrations comparable to those Ni concentrations estimated for the Archean ocean (0.04–0.4 μM). Only after the secular decline in oceanic Ni concentrations around 2.7 Ga, together with increasing PO_4^{3-} concentrations (Robbins et al., 2016), would these inhibitory effects have eased, facilitating the ecological expansion of cyanobacteria and the subsequent rise of atmospheric O_2.

CRediT authorship contribution statement

Carolin L. Dreher: Writing – review & editing, Writing – original draft, Visualization, Methodology, Investigation, Formal analysis, Data curation, Conceptualization. **Manuel Schad:** Writing – review & editing, Supervision, Conceptualization. **Andreas Kappler:** Writing – review & editing, Writing – original draft, Validation, Supervision, Resources, Project administration, Methodology, Funding acquisition, Conceptualization. **Kurt O. Konhauser:** Writing – review & editing, Writing – original draft, Validation, Supervision, Resources, Methodology, Funding acquisition, Conceptualization.

Declaration of competing interest

The authors declare that they have no known competing financial interests or personal relationships that could have appeared to influence the work reported in this paper.

Acknowledgements

J. López Rivoldi and M. Mergenthaler are acknowledged for their experimental support. We would like to thank Dr. Sören Drabesch, Dr. Muammar Mansor and Dr. Martina Bottaro for the ICP-MS measurements. The authors would further like to thank F. Schädler and L. Grimm for maintenance and help in the laboratory. Dr. J. P. Duda, Dr. E. Runge, Dr. A. Ilin Moskalenko, and Y. Li, are acknowledged for fruitful discussions on experimental design and data interpretation.

We would like to thank the Deutsche Forschungsgemeinschaft (DFG, German Research Foundation) for supporting grants for this project to AK, project ID AOBJ: 669932.

Appendix A. Supplementary data

Supplementary data to this article can be found online at https://doi.org/10.1016/j.chemgeo.2026.123499.

Data availability

Data will be made available on request.

References

Abuladze, M., Asatiani, N., Kartvelishvili, T., Krivonos, D., Popova, N., Safonov, A., Sapojnikova, N., Yushin, N., Zinicovscaia, I., 2023. Adaptive mechanisms of *Shewanella xiamenensis* DCB 2-1 metallophilicity. Toxics 11, 304. https://doi.org/10.3390/toxics11040304.

Awasthi, M., Chand Rai, L., 2004. Effect of nickel and cadmium on ammonium uptake kinetics of free and immobilized cells of *Anacystis nidulans*. Acta Hydrochim. Hydrobiol. 32, 149–153. https://doi.org/10.1002/aheh.200300525.

Azeez, P.A., Banerjee, D.K., 1991. Nickel uptake and toxicity in cyanobacteria. Toxicol. Environ. Chem. 30, 43–50. https://doi.org/10.1080/02772249109357639.

Bekker, A., Holland, H.D., Wang, P.-L., Rumble, D., Stein, H.J., Hannah, J.L., Coetzee, L. L., Beukes, N.J., 2004. Dating the rise of atmospheric oxygen. Nature 427, 117–120. https://doi.org/10.1038/nature02260.

Beukes, N.J., 1973. Precambrian iron-formations of Southern Africa. Econ. Geol. 68, 960–1004. https://doi.org/10.2113/gsecongeo.68.7.960.

Bishop, B.A., Flynn, S.L., Warchola, T.J., Alam, Md.S., Robbins, L.J., Liu, Y., Owttrim, G. W., Alessi, D.S., Konhauser, K.O., 2019. Adsorption of biologically critical trace elements to the marine cyanobacterium *Synechococcus* sp. PCC 7002: Implications

for marine trace metal cycling. Chem. Geol. 525, 28–36. https://doi.org/10.1016/j.chemgeo.2019.05.021.
Bjerrum, C.J., Canfield, D.E., 2002. Ocean productivity before about 1.9 Gyr ago limited by phosphorus adsorption onto iron oxides. Nature 417, 159–162. https://doi.org/10.1038/417159a.
Bruland, K.W., Lohan, M.C., 2003. Controls of trace metals in seawater. Treat. Geochem. 6, 23–47. https://doi.org/10.1016/B0-08-043751-6/06105-3.
Buchman, J.T., Bennett, E.A., Wang, C., Tamijani, A.A., Bennett, J.W., Hudson, B.G., Green, C.M., Clement, P.L., Zhi, B., Henke, A.H., Laudadio, E.D., Mason, S.E., Hamers, R.J., Klaper, R.D., Haynes, C.L., 2020. Nickel enrichment of next-generation NMC nanomaterials alters material stability, causing unexpected dissolution behavior and observed toxicity to *S. oneidensis* MR-1 and *D. magna*. Environ. Sci. Nano 7, 571–587. https://doi.org/10.1039/C9EN01074B.
Chen, X., Ostrander, C.M., Holdaway, B.J., Kendall, B., Anbar, A.D., Nielsen, S.G., Owens, J.D., 2025. Transient marine bottom water oxygenation on continental shelves by 2.65 billion years ago. Nat. Geosci. 18, 423–429. https://doi.org/10.1038/s41561-025-01681-9.
Cloud, P., 1965. Significance of the gunflint (Precambrian) microflora. Science 148, 27–35. https://doi.org/10.1126/science.148.3666.27.
Cloud, P., 1973. Paleoecological significance of the Banded Iron-Formation. Econ. Geol. 68, 1135–1143. https://doi.org/10.2113/gsecongeo.68.7.1135.
Dreher, C.L., Schad, M., Duda, J.-P., Fischer, S., Shuster, J., Li, Y., Konhauser, K.O., Kappler, A., 2025. Impact of silica on the identity of minerals formed in Archean oceans during Fe cycling by cyanobacteria and iron(III)-reducing bacteria. Geochim. Cosmochim. Acta 404, 202–222. https://doi.org/10.1016/j.gca.2025.07.023.
Dreher, C.L., Cirpka, O.A., Schad, M., Konhauser, K.O., Kappler, A., 2026. Survival of cyanobacteria and mitigation of Fe(II) toxicity effects in a silica-rich Archean Ocean. Nat. Commun. 17, 1987. https://doi.org/10.1038/s41467-026-69826-x.
Eickhoff, M., Obst, M., Schröder, C., Hitchcock, A.P., Tyliszczak, T., Martinez, R.E., Robbins, L.J., Konhauser, K.O., Kappler, A., 2014. Nickel partitioning in biogenic and abiogenic ferrihydrite: the influence of silica and implications for ancient environments. Geochim. Cosmochim. Acta 140, 65–79. https://doi.org/10.1016/j.gca.2014.05.021.
Fanning, K.A., Pilson, M.E., 1973. On the spectrophotometric determination of dissolved silica in natural waters. Anal. Chem. 45, 136–140. https://doi.org/10.1021/ac60323a021.
Flynn, S.L., Szymanowski, J.E.S., Fein, J.B., 2014. Modeling bacterial metal toxicity using a surface complexation approach. Chem. Geol. 374–375, 110–116. https://doi.org/10.1016/j.chemgeo.2014.03.010.
Halama, M., Swanner, E.D., Konhauser, K.O., Kappler, A., 2016. Evaluation of siderite and magnetite formation in BIFs by pressure–temperature experiments of Fe(III) minerals and microbial biomass. Earth Planet. Sci. Lett. 450, 243–253. https://doi.org/10.1016/j.epsl.2016.06.032.
Han, M., Wang, H., Zhou, J., Liu, K., Wang, N., Chen, X., Liu, Y., Liang, H., 2025. Introducing Lewis base-phosphate to boost neutral seawater splitting in anion exchange membrane electrolyzer. Adv. Funct. Mater. 35, 2415143. https://doi.org/10.1002/adfm.202415143.
Hausinger, R.P., 1987. Nickel utilization by Microorganisms. Microbiol. Rev. 51, 22–42.
Hegler, F., Posth, N.R., Jiang, J., Kappler, A., 2008. Physiology of phototrophic iron(II)-oxidizing bacteria: implications for modern and ancient environments: physiology of phototrophic iron(II)-oxidizing bacteria. FEMS Microbiol. Ecol. 66, 250–260. https://doi.org/10.1111/j.1574-6941.2008.00592.x.
Hemmingsson, C., Pitcairn, I.K., Fru, E.C., 2018. Evaluation of phosphate-uptake mechanisms by Fe(III) (oxyhydr)oxides in early Proterozoic oceanic conditions. Environ. Chem. 15, 18–28. https://doi.org/10.1071/EN17124.
Huang, H., Ji, X.-B., Cheng, L.-Y., Zhao, F.-J., Wang, P., 2021. Free radicals produced from the oxidation of ferrous sulfides promote the remobilization of cadmium in paddy soils during drainage. Environ. Sci. Technol. 55, 9845–9853. https://doi.org/10.1021/acs.est.1c00576.
Huertas, M., López-Maury, L., Giner-Lamia, J., Sánchez-Riego, A., Florencio, F., 2014. Metals in cyanobacteria: analysis of the copper, nickel, cobalt and arsenic homeostasis mechanisms. Life 4, 865–886. https://doi.org/10.3390/life4040865.
Hunter, B.M., Hieringer, W., Winkler, J.R., Gray, H.B., Müller, A.M., 2016. Effect of interlayer anions on [NiFe]-LDH nanosheet water oxidation activity. Energy Environ. Sci. 9, 1734–1743. https://doi.org/10.1039/C6EE00377J.
Jones, C., Nomosatryo, S., Crowe, S.A., Bjerrum, C.J., Canfield, D.E., 2015. Iron oxides, divalent cations, silica, and the early earth phosphorus crisis. Geology 43, 135–138. https://doi.org/10.1130/G36044.1.
Kida, K., Shigematsu, T., Kijima, J., Numaguchi, M., Mochinaga, Y., Abe, N., Morimura, S., 2001. Influence of Ni2+ and Co2+ on methanogenic activity and the amounts of coenzymes involved in methanogenesis. J. Biosci. Bioeng. 91, 590–595. https://doi.org/10.1016/S1389-1723(01)80179-1.
Kipp, M.A., Stüeken, E.E., 2017. Biomass recycling and Earth's early phosphorus cycle. Sci. Adv. 3, 4795. https://doi.org/10.1126/sciadv.aao4795.
Köhler, I., Konhauser, K.O., Papineau, D., Bekker, A., Kappler, A., 2013. Biological carbon precursor to diagenetic siderite with spherical structures in iron formations. Nat. Commun. 4, 1–7. https://doi.org/10.1038/ncomms2770.
Konhauser, K.O., Newman, D.K., Kappler, A., 2005. The potential significance of microbial Fe(III) reduction Fe (III) reduction in BIFs Blackwell Publishing Ltd ORIGINAL ARTICLE during deposition of Precambrian banded iron formations. Geobiology 3, 167–177. https://doi.org/10.1111/j.1472-4669.2005.00055.x.
Konhauser, K.O., Lalonde, S.V., Amskold, L., Holland, H.D., 2007. Was there really an Archean phosphate crisis? Science 315, 1234. https://doi.org/10.1126/science.1136328.
Konhauser, K.O., Pecoits, E., Lalonde, S.V., Papineau, D., Nisbet, E.G., Barley, M.E., Arndt, N.T., Zahnle, K., Kamber, B.S., 2009. Oceanic nickel depletion and a methanogen famine before the Great Oxidation Event. Nature 458, 750–753. https://doi.org/10.1038/nature07858.
Konhauser, K.O., Robbins, L.J., Pecoits, E., Peacock, C., Kappler, A., Lalonde, S.V., 2015. The Archean nickel famine revisited. Astrobiology 15, 804–815. https://doi.org/10.1089/ast.2015.1301.
Konhauser, K.O., Planavsky, N.J., Hardisty, D.S., Robbins, L.J., Warchola, T.J., Haugaard, R., Lalonde, S.V., Partin, C.A., Oonk, P.B.H., Tsikos, H., Lyons, T.W., Bekker, A., Johnson, C.M., 2017. Iron formations: a global record of Neoarchaean to Palaeoproterozoic environmental history. Earth Sci. Rev. 172, 140–177. https://doi.org/10.1016/j.earscirev.2017.06.012.
Kretz, C.B., Bell, D.W., Lomas, D.A., Lomas, M.W., Martiny, A.C., 2015. Influence of growth rate on the physiological response of marine *Synechococcus* to phosphate limitation. Front. Microbiol. 6. https://doi.org/10.3389/fmicb.2015.00085.
Kuffner, I., Paul, V., 2001. Effects of nitrate, phosphate and iron on the growth of macroalgae and benthic cyanobacteria from Cocos Lagoon, Guam. Mar. Ecol. Prog. Ser. 222, 63–72. https://doi.org/10.3354/meps222063.
Kump, L.R., Barley, M.E., 2007. Increased subaerial volcanism and the rise of atmospheric oxygen 2.5 billion years ago. Nature 448, 1033–1036. https://doi.org/10.1038/nature06058.
Lehtimaki, J., Moisander, P., Sivonen, K., Kononen, K., 1997. Growth, nitrogen fixation, and nodularin production by two Baltic Sea cyanobacteria. Appl. Environ. Microbiol. 63, 1647–1656. https://doi.org/10.1128/aem.63.5.1647-1656.1997.
Li, Y., Konhauser, K.O., Cole, D.R., Phelps, T.J., 2011. Mineral ecophysiological data provide growing evidence for microbial activity in banded-iron formations. Geol. Soc. Am. Bull. 39, 707–710. https://doi.org/10.1130/G32003.1.
Li, Y.-L., Konhauser, K.O., Zhai, M., 2017. The formation of magnetite in the early Archean oceans. Earth Planet. Sci. Lett. 466, 103–114. https://doi.org/10.1016/j.epsl.2017.03.013.
Li, Y., Sutherland, B.R., Ilin, M., Schad, M., Robbins, L., Kappler, A., Yusta, I., Sánchez-España, J., Owttrim, G.W., Dreher, C., Smith, A.J.B., Alessi, D., Gringas, M.K., Konhauser, K., 2024. Cyanobacteria-ferrihydrite aggregates, BIF sedimentation and implications for Archaean- Palaeoproterozoic seawater geochemistry. S. Afr. J. Geol. 127, 359. https://doi.org/10.25131/sajg.127.0010.
Liang, X., Stüeken, E.E., Alessi, D.S., Konhauser, K.O., Li, L., 2025. A seawater oxygen oscillation recorded by iron formations prior to the Great Oxidation Event. Nat. Geosci. 18, 417–422. https://doi.org/10.1038/s41561-025-01683-7.
Lovley, D.R., Phillips, E.J.P., 1988. Novel mode of microbial energy metabolism: organic carbon oxidation coupled to dissimilatory reduction of iron or manganese. Appl. Environ. Microbiol. 54, 1472–1480.
Macomber, L., Hausinger, R.P., 2011. Mechanisms of nickel toxicity in microorganisms†. Metallomics 3, 1153–1162. https://doi.org/10.1039/c1mt00063b.
Niu, Q., Gao, F.-Y., Sun, X., Zheng, Y., Qiao, S.-Z., 2026. Chloride-mediated electron buffering on Ni-Fe anodes for ampere-level alkaline seawater electrolysis. Adv. Funct. Mater., 2504872 https://doi.org/10.1002/adfm.202504872.
Nohomovich, B., Nguyen, B.T., Quintanilla, M., Lee, L.H., Murray, S.R., Chu, T.-C., 2013. Physiological effects of nickel chloride on the freshwater cyanobacterium Synechococcus sp. IU 625. Adv. Biosci. Biotechnol. 4, 10–14. https://doi.org/10.4236/abb.2013.47A2002.
Ozaki, K., Reinhard, C.T., Tajika, E., 2019. A sluggish mid-Proterozoic biosphere and its effect on Earth's redox balance. Geobiology 17, 3–11. https://doi.org/10.1111/gbi.12317.
Pantke, C., Obst, M., Benzerara, K., Morin, G., Ona-Nguema, G., Dippon, U., Kappler, A., 2012. Green rust formation during Fe(II) oxidation by the nitrate-reducing Acidovorax sp. strain BoFeN1. Environ. Sci. Technol. 46, 1439–1446. https://doi.org/10.1021/es2016457.
Percak-Dennett, E.M., Beard, B.L., Xu, H., Konishi, H., Johnson, C.M., Roden, E.E., 2011. Iron isotope fractionation during microbial dissimilatory iron oxide reduction in simulated Archaean seawater. Geobiology 9, 205–220. https://doi.org/10.1111/j.1472-4669.2011.00277.x.
Pérez, A.A., Rodionov, D.A., Bryant, D.A., 2016. Identification and regulation of genes for cobalamin transport in the cyanobacterium Synechococcus sp. Strain PCC 7002. J. Bacteriol. 198, 2753–2761. https://doi.org/10.1128/jb.00476-16.
Planavsky, N., Bekker, A., Rouxel, O.J., Kamber, B., Hofmann, A., Knudsen, A., Lyons, T. W., 2010. Rare Earth Element and yttrium compositions of Archean and Paleoproterozoic Fe formations revisited: New perspectives on the significance and mechanisms of deposition. Geochim. Cosmochim. Acta 74, 6387–6405. https://doi.org/10.1016/j.gca.2010.07.021.
Posth, N.R., Konhauser, K.O., Kappler, A., 2013. Microbiological processes in banded iron formation deposition. Sedimentology 60, 1733–1754. https://doi.org/10.1111/sed.12051.
Poulton, S.W., Bekker, A., Cumming, V.M., Zerkle, A.L., Canfield, D.E., Johnston, D.T., 2021. A 200-million-year delay in permanent atmospheric oxygenation. Nature 592, 232–236. https://doi.org/10.1038/s41586-021-03393-7.
Rasmussen, B., Muhling, J.R., Suvorova, A., Fischer, W.W., 2021. Apatite nanoparticles in 3.46–2.46 Ga iron formations: evidence for phosphorus-rich hydrothermal plumes on early Earth. Geology. https://doi.org/10.1130/G48374.1.
Rego, E.S., Busigny, V., Lalonde, S.V., Rossignol, C., Babinski, M., Philippot, P., 2023. Low-phosphorus concentrations and important ferric hydroxide scavenging in Archean seawater. PNAS Nexus 2, pgad025. https://doi.org/10.1093/pnasnexus/pgad025.
Reinhard, C.T., Planavsky, N.J., Gill, B.C., Ozaki, K., Robbins, L.J., Lyons, T.W., Fischer, W.W., Wang, C., Cole, D.B., Konhauser, K.O., 2017. Evolution of the global phosphorus cycle. Nature 541, 386–389. https://doi.org/10.1038/nature20772.
Robbins, L.J., Lalonde, S.V., Planavsky, N.J., Partin, C.A., Reinhard, C.T., Kendall, B., Scott, C., Hardisty, D.S., Gill, B.C., Alessi, D.S., Dupont, C.L., Saito, M.A., Crowe, S. A., Poulton, S.W., Bekker, A., Lyons, T.W., Konhauser, K.O., 2016. Trace elements at

the intersection of marine biological and geochemical evolution. Earth Sci. Rev. 163, 323–348. https://doi.org/10.1016/j.earscirev.2016.10.013.
Roden, E.E., Edmonds, J.W., 1997. Phosphate mobilization in iron-rich anaerobic sediments: microbial Fe(III)oxide reduction versus iron-sulfide formation. Arch. Hydrobiol. 193, 347–378. https://doi.org/10.1127/archiv-hydrobiol/139/1997/347.
Sabour, B., Mohammed, Loudiki, Vasconcelos, V., 2009. Growth responses of Microcystis ichthyoblabe Kützing and Anabaena aphanizomenoides Forti (cyanobacteria) under different nitrogen and phosphorus conditions. Chem. Ecol. 25, 337–344. https://doi.org/10.1080/02757540903193130.
Sakamoto, T., Bryant, D.A., 2001. Requirement of nickel as an essential micronutrient for the utilization of urea in the marine cyanobacterium Synechococcus sp. PCC 7002. Microbes Environ. 16, 177–184. https://doi.org/10.1264/jsme2.2001.177.
Sánchez-Baracaldo, P., Bianchini, G., Wilson, J.D., Knoll, A.H., 2022. Cyanobacteria and biogeochemical cycles through Earth history. Trends Microbiol. 30, 143–157. https://doi.org/10.1016/j.tim.2021.05.008.
Scanlan, D.J., Silman, N.J., Donald, K.M., Wilson, W.H., Carr, N.G., Joint, I., Mann, N.H., 1997. An immunological approach to detect phosphate stress in populations and single cells of photosynthetic picoplankton. Appl. Environ. Microbiol. 63, 2411–2420. https://doi.org/10.1128/aem.63.6.2411-2420.1997.
Schad, M., Byrne, J.M., ThomasArrigo, L.K., Kretzschmar, R., Konhauser, K.O., Kappler, A., 2022. Microbial Fe cycling in a simulated Precambrian Ocean environment: implications for secondary mineral (trans)formation and deposition during BIF genesis. Geochim. Cosmochim. Acta 331, 165–191. https://doi.org/10.1016/j.gca.2022.05.016.
Schluchter, W.M., Bryant, D.A., 1992. Molecular characterization of ferredoxin-NADP+ oxidoreductase in cyanobacteria: cloning and sequence of the petH gene of Synechococcus sp. PCC 7002 and studies on the gene product. Biochemistry 31, 3092–3102. https://doi.org/10.1021/bi00127a009.
Schönheit, P., Moll, J., Thauer, R.K., 1979. Nickel, cobalt, and molybdenum requirement for growth of Methanobacterium thermoautotrophicum. Arch. Microbiol. 123, 105–107. https://doi.org/10.1007/BF00403508.
Selão, T.T., Włodarczyk, A., Nixon, P.J., Norling, B., 2019. Growth and selection of the cyanobacterium *Synechococcus* sp. PCC 7002 using alternative nitrogen and phosphorus sources. https://doi.org/10.1101/603373.
Shukla, M.K., Tripathi, R.D., Sharma, N., Dwivedi, S., Mishra, S., Singh, R., Shukla, O.P., Rai, U.N., 2009. Responses of cyanobacterium Anabaena doliolum during nickel stress. J. Environ. Biol. 30, 871–876.
Sundman, A., Karlsson, T., Sjöberg, S., Persson, P., 2016. Impact of iron–organic matter complexes on aqueous phosphate concentrations. Chem. Geol. 426, 109–117. https://doi.org/10.1016/j.chemgeo.2016.02.008.
Thiel, T., 1988. Phosphate transport and arsenate resistance in the cyanobacterium *Anabaena variabilis*. J. Bacteriol. 170, 1143–1147. https://doi.org/10.1128/jb.170.3.1143-1147.1988.
Trendall, A.F., 2002. The significance of iron-formation in the Precambrian stratigraphic record. Spec. Publ. Int. Assoc. Sedimentol. 33, 33–66. https://doi.org/10.1002/9781444304312.ch3.
Trindade, I.B., Fonseca, B.M., Catarino, T., Matias, P.M., Moe, E., Louro, R.O., 2024. Flavin-containing siderophore-interacting protein of *Shewanella putrefaciens* DSM 9451 reveals substrate specificity in ferric-siderophore reduction. https://doi.org/10.1101/2024.05.13.594011.
Vakili, M., Rafatullah, M., Yuan, J., Zwain, H.M., Mojiri, A., Gholami, Z., Gholami, F., Wang, W., Giwa, A.S., Yu, Y., Cagnetta, G., Yu, G., 2021. Nickel ion removal from aqueous solutions through the adsorption process: a review. Rev. Chem. Eng. 37, 755–778. https://doi.org/10.1515/revce-2019-0047.
Wang, H.Kang, Wood, J.M., 1984. Bioaccumulation of nickel by algae. Environ. Sci. Technol. 18, 106–109. https://doi.org/10.1021/es00120a011.
Wu, L., Percak-Dennett, E.M., Beard, B.L., Roden, E.E., Johnson, C.M., 2012. Stable iron isotope fractionation between aqueous Fe(II) and model Archean Ocean Fe–Si coprecipitates and implications for iron isotope variations in the ancient rock record. Geochim. Cosmochim. Acta 84, 14–28. https://doi.org/10.1016/j.gca.2012.01.007.
Xu, Y., Axe, L., Boonfueng, T., Tyson, T.A., Trivedi, P., Pandya, K., 2007. Ni(II) complexation to amorphous hydrous ferric oxide: an X-ray absorption spectroscopy study. J. Colloid Interface Sci. 314, 10–17. https://doi.org/10.1016/j.jcis.2007.05.037.
Yan, J., Jiang, T., Yao, Y., Lu, S., Wang, Q., Wei, S., 2016. Preliminary investigation of phosphorus adsorption onto two types of iron oxide-organic matter complexes. J. Environ. Sci. (China) 42, 152–162. https://doi.org/10.1016/j.jes.2015.08.008.
Zambelli, B., Musiani, F., Benini, S., Ciurli, S., 2011. Chemistry of Ni2+ in urease: sensing, trafficking, and catalysis. Acc. Chem. Res. 44, 520–530. https://doi.org/10.1021/ar200041k.